JOURNAL OF GEOPHYSICAL RESEARCH, VOL. 96, NO. B4, PAGES 6291–6302, APRIL 10, 1991

High-Frequency Spectral Falloff of Earthquakes, Fractal Dimension of Complex Rupture, *b* Value, and the Scaling of Strength on Faults

ARTHUR FRANKEL

U.S. Geological Survey, Reston, Virginia

The high-frequency falloff $\omega^{-\gamma}$ of earthquake displacement spectra and the b value of aftershock sequences are attributed to the character of spatially varying strength along fault zones. I assume that the high frequency energy of a main shock is produced by a self-similar distribution of subevents, where the number of subevents with radii greater than R is proportional to R^{-D}, D being the fractal dimension. In this model, an earthquake is composed of a hierarchical set of smaller earthquakes. The static stress drop is parameterized to be proportional to R^{η}, and strength is assumed to be proportional to static stress drop. I find that a distribution of subevents with $D = 2$ and stress drop independent of seismic moment ($\eta = 0$) produces a main shock with an ω^{-2} falloff, if the subevent areas fill the rupture area of the main shock. By equating subevents to "islands" of high stress of a random, self-similar stress field on a fault, I relate D to the scaling of strength on a fault, such that $D = 2 - \eta$. Thus $D = 2$ corresponds to constant stress drop scaling ($\eta = 0$) and scale-invariant fault strength. A self-similar model of aftershock rupture zones on a fault is used to determine the relationship between the b value, the size distribution of aftershock rupture zones, and the scaling of strength on a fault. The b value for aftershock sequences on a fault is found to equal $(3 - 1.5\eta)/(3 + \eta)$. Therefore this model indicates that the typically observed spectral falloffs of ω^{-2} and b values of 1 can be entirely caused by scale-invariant strength ($\eta = 0$) along fault zones.

INTRODUCTION

Variations in rock type, bends, steps, splays, and many other complications along fault zones cause their effective shear strength to vary spatially. This paper considers two manifestations of heterogeneous fault strength related to earthquake occurrence. The first is the generation of high-frequency seismic energy by earthquakes, which can be quantified by the high-frequency falloff of their displacement spectra. It has long been recognized that the high-frequency radiation from earthquakes could be produced by complications on the fault plane at scales smaller than the overall rupture dimension [e.g., *Housner*, 1955; *Haskell*, 1964]. As discussed below, this high-frequency energy can be viewed as a result of rupture of subevents on small patches of relatively high stress on a fault plane. Understanding the character of the high-frequency radiation of earthquakes is important to several major efforts in seismology and engineering. High-frequency strong ground motion (>1 Hz) is a major cause of damage to many types of buildings. Many schemes developed to discriminate underground nuclear explosions from earthquakes rely on their relative excitation of high-frequency seismic energy.

The second manifestation of fault zone heterogeneity addressed here is the frequency of occurrence of aftershocks as a function of their magnitude, which is parameterized by the b value [*Richter*, 1958]. Aftershock rupture zones can also be viewed as areas of relatively high stress on a fault, similar in some respects to subevents that occur during individual earthquakes. The b value is important for estimating the expected recurrence of earthquakes over a region. Thus, understanding the underlying cause of the b value also ties in with seismic hazard assessment.

Displacement spectra of earthquakes typically exhibit a high-frequency falloff above the corner frequency that is proportional to ω^{-2}, where ω is the angular frequency [e.g., *Housner*, 1947; *Aki*, 1967; *Hanks*, 1981; *Chael*, 1987]. This corresponds to an acceleration spectrum that is flat for frequencies above the corner frequency. Many models of the earthquake source have been developed to try to explain this high-frequency spectral character. *Brune* [1970] proposed a source model with an instantaneous stress pulse that he found to produce a displacement spectrum with an ω^{-2} falloff. However, later studies using dynamic models demonstrated that rupture nucleation generates high-frequency energy that is proportional to ω^{-3} [e.g., *Madariaga*, 1976] and that smooth rupture propagation generates relatively little high-frequency energy [*Madariaga*, 1977]. Thus models with smooth ruptures cannot produce the requisite amounts of high-frequency observed in actual seismograms (T. H. Heaton, unpublished manuscript, 1990). For simple ruptures on fault planes with uniform strength and stress, it is necessary to have abrupt stopping behavior simultaneously over the perimeter of the fault to generate ω^{-2} falloffs [*Madariaga*, 1976].

Hanks [1979] and *Andrews* [1981] proposed that the ω^{-2} spectral falloff was a manifestation of complexity in the rupture process caused by heterogeneous stress relief along the fault plane. That point of view is taken in this paper. *Hanks* [1979] suggested that the high-frequency spectral falloff could be related to the scaling of seismic stress drop with moment and the b value of earthquake sequences. He found that a stress drop independent of moment produced a high-frequency decay of ω^{-2}. To make this conclusion, *Hanks* [1979] assumed that the high-frequency spectral amplitude of an earthquake at any given frequency was controlled by stress variations on the fault with a scale length inversely proportional to that frequency. *Andrews* [1981] quantified the relation between the high-frequency rolloff and the fractal dimension of the stress drop along the fault, based on an analysis of the spatial Fourier transforms of the

Paper number 91JB00237.

slip velocity and stress. He assumed that the slip velocity had the same power law dependency in time as in space.

One purpose of this paper is to show that the exponent (γ) of the high-frequency spectral falloff ($\omega^{-\gamma}$) can indeed be determined by the scaling of strength with distance along the fault plane, as suggested by *Hanks* [1979] and *Andrews* [1981]. I develop a self-similar model of complex rupture where an earthquake is composed of subevents with different sizes. These subevents are themselves composed of subevents, and so on. In this model, an earthquake is made up of a hierarchical set of smaller earthquakes. I show how such a model can link the high-frequency spectral falloff of earthquakes with the scaling of strength along faults. In this analysis, I assume that the stress drop of earthquakes or subevents on a fault is proportional to fault strength, which varies with position along a fault.

I first show that the high-frequency spectral falloff of the main shock can be determined by the size distribution of the subevents which compose that earthquake. This size distribution of subevents defines the fractal dimension D [*Mandelbrot*, 1977]. By considering stress a self-similar random function of position along the fault, I then demonstrate that the fractal dimension of subevents is controlled by the scaling of strength or stress drop on the fault. From this analysis, I find that a scale-invariant fault strength produces a rupture with a fractal dimension of two and an ω^{-2} spectral falloff, if the subevent areas fill the main shock rupture area. *Hanks* [1979] and *Andrews* [1981] also found that constant stress drop scaling led to an ω^{-2} falloff, using different methodologies.

The fractal distribution of subevent sizes in this model of complex rupture is consistent with observations of fault properties. Observations of surface faulting for large earthquakes indicate that fault zone complications occur on a variety of scales [e.g., *Tchalenko and Ambraseys*, 1970], with shear zone features at small scale lengths (centimeters) looking like miniature versions of large-scale features (kilometers). Measurements of the fractal dimension of the surface trace of the San Andreas fault by *Okubo and Aki* [1987] and *Aviles et al.* [1987] have attempted to quantify its bends and subsidiary faulting for a wide range of length scales. Random topography on the contact surfaces of a fault can also be described by fractals [*Brown and Scholz*, 1985]. All of these complications can produce a self-similar variation in effective strength and stress on the fault plane. *Scholz and Aviles* [1986] discussed the implications of the fractal geometry of faulting to the generation of high-frequency seismic radiation. Some work has been done incorporating failure at different length scales into models of earthquake sources [e.g., *Blandford*, 1975] and simulations of complex rupture [*Boatwright and Quin*, 1986]. *Smalley et al.* [1985] used a renormalization group method to study how earthquake rupture can expand from the successive failure of nested asperities with different sizes.

Another goal of this paper is to demonstrate that b values of aftershock sequences on a fault can also be a function of the scaling of strength on faults. It is generally observed that b values of aftershock sequences are, on average, equal to 1 [see *Utsu*, 1971]. Many studies have shown that a b value of 1 can be an expression of the size distribution of earthquake rupture zones on a fault. These studies find that a b value of 1 will result if the number of rupture zones with a given area is inversely proportional to that area [*Kanamori and Anderson*, 1975; *Hanks*, 1977; *Andrews*, 1980; *Aki*, 1981; *Turcotte*, 1989; *Rundle*, 1989]. In this paper, I show that such a size distribution of rupture areas can arise from a scale-invariant fault strength.

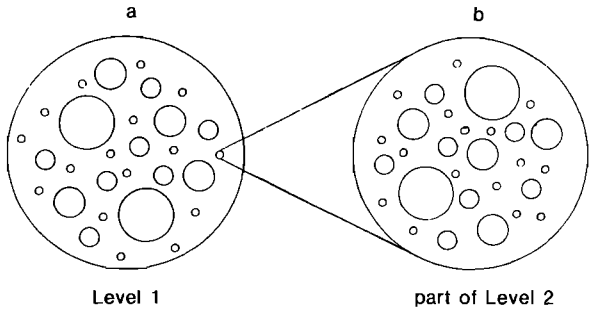

Fig. 1. (*a*) A simplified example of a rupture model with a continuous, self-similar distribution of subevent rupture areas. Rupture zones of subevents are shown by different sizes of circles. The outermost circle represents the rupture area of the main shock. The rupture zones shown in Figure 1*a* are the level 1 subevents. (*b*) A blow-up of one of the subevents in Figure 1*a*, showing that it contains its own self-similar distribution of subevents (level 2).

The central result of this paper is that the high-frequency spectral falloff of earthquakes, the size distribution of subevent and aftershock rupture areas, and the b value of aftershock sequences can all be determined from the scaling of strength on fault zones.

Model For Complex Rupture

In this paper, I use a model of complex rupture where an earthquake is composed of a set of subevents of various rupture sizes, each of which is itself a complex earthquake. Figure 1 is a simplified picture of such a rupture model. Figure 1*a* shows the subevents within the main shock that are not contained in any other subevents, designated here as level 1 subevents. The size distribution of these level 1 subevent areas is self-similar. That is, taking a small part of the main shock area and enlarging it by some factor will produce a distribution of subevent areas that is statistically identical to the original. I assume that the radiation of these subevents generates the high-frequency radiation of the main shock. The rupture areas of subevents on any particular level do not overlap.

Within each of the level 1 subevent areas shown in Figure 1*a* there is a self-similar distribution of subevents (see Figure 1*b*), denoted here as level 2 subevents. In turn, each one of these level 2 subevents has its own subevents (level 3), and so on. So each level 1 subevent is composed of a hierarchy of smaller subevents within it. The sizes of the subevents correspond to different scales of stress/strength variations on the fault plane. Larger-scale fluctuations of stress will have smaller-scale variations within them. As described in more detail below, the spaces in between the subevents at any given level do not have zero stress. I show in a later section that this nested, self-similar distribution of subevents can be understood as the expression of strength being a random self-similar function of position on the fault plane.

The size distribution of the subevents can be quantified by its fractal dimension [*Mandelbrot*, 1977]. For the model shown in Figure 1, the distribution of level 1 subevents is specified by

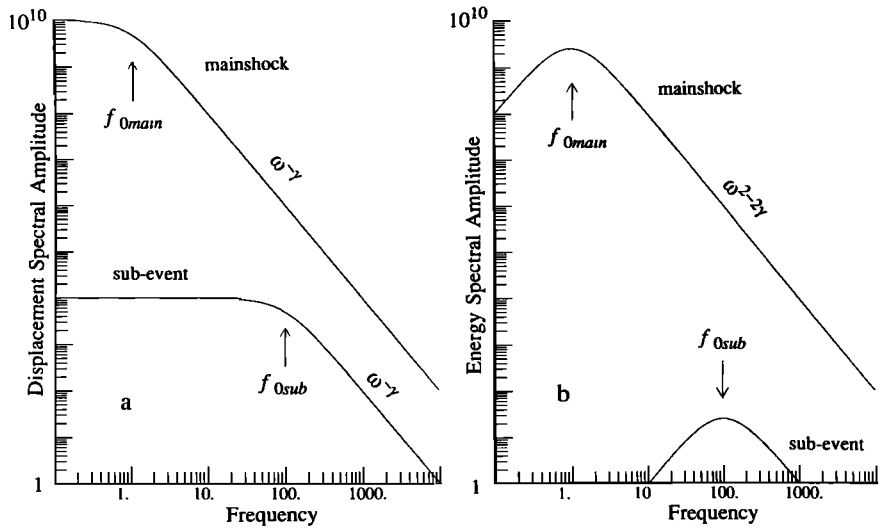

Fig. 2. (*a*) Displacement spectra for a main shock and one of its subevents. For this example, the stress drops of the main shock and subevent are equal and the high-frequency spectral falloff is ω^{-2}. The $f_{0\text{main}}$ and $f_{0\text{sub}}$ are corner frequencies of main shock and subevent. Low-frequency spectral levels are proportional to seismic moments $M_{0\text{main}}$ and $M_{0\text{sub}}$. Axes for spectral amplitude and frequency are in arbitrary units. (*b*) Energy spectra for main shock and subevent.

$$\frac{dN}{d(\ln R_{\text{sub}})} = p\left(\frac{R_{\text{sub}}}{R_{\text{main}}}\right)^{-D}, \tag{1}$$

where D is the fractal dimension, N is the number of level 1 subevents, R_{sub} is subevent radius, R_{main} is the radius of the main shock rupture zone, and p is a constant of proportionality. The subevents have a continuous size distribution. The $dN/d(\ln R_{\text{sub}})$ describes the probability distribution of subevents over a logarithmic interval of radius. From (1), the number $N(R)$ of level 1 subevents with radii greater than R is

$$N(R) \propto \int_R^{R_{\max}} R_{\text{sub}}^{-D}\, d(\ln R_{\text{sub}}).$$

$R_{\max}$ is the maximum subevent size for the distribution. Since $d(\ln R_{\text{sub}}) = R_{\text{sub}}^{-1}\, dR_{\text{sub}}$, this equation becomes

$$N(R) \propto \int_R^{R_{\max}} R_{\text{sub}}^{-D-1}\, dR_{\text{sub}}.$$

After integration, the number of level 1 subevents with radii larger than R is found to be

$$N(R) \propto R^{-D} + C, \tag{2}$$

where C is a constant.

Because the model in Figure 1 is self-similar, the distribution in (1) and (2) also describes the number of level 2 subevents in a level 1 subevent with size R_1. In (1) we would substitute R_1 for R_{main}. The same size-distribution would apply for subevents within other subevents at all levels.

I assume that there is a minimum size $R_{\min}$ for the complex subevents. $R_{\min}$ is not the minimum source radius. Complex subevents with $R_{\min}$ would be composed of smaller subevents with simple ruptures. $R_{\min}$ is not meant to correspond to the critical crack length generally found in dynamic models of faulting [e.g., *Dieterich*, 1986]. The self-similarity of the rupture model is valid for length scales greater than or equal to $R_{\min}$.

The analysis in this paper is based on other assumptions, such as the corner frequency of a subevent is inversely proportional to its source radius. This means that the dominant period of the radiated energy is proportional to the source radius. I assume that the spectral amplitude above the corner frequency decays as a power of frequency. The spectra of the subevents have the same high-frequency rolloff regardless of source size. Because of the self-similarity of the rupture model, the subevents have the same high-frequency falloff as the main shock. The shape of the displacement spectrum $\Omega(f)$ of the main shock or any subevent is given by

$$\Omega(f) \propto \frac{M_0}{1 + (f/f_0)^{\gamma}}, \tag{3}$$

where M_0 is the seismic moment of the subevent, f_0 denotes its corner frequency, and f is frequency. Figure 2*a* shows displacement spectra for a main shock and one of its subevents. For simplicity, I also assume that the rupture zones are circular. The spectrum of the radiated energy is proportional to the square of the velocity spectral amplitude, so

$$E(f) \propto f^2\Omega^2(f). \tag{4}$$

Figure 2*b* depicts the energy spectra for the main shock and one of its subevents, corresponding to the displacement spectra in Figure 2*a*. At high frequencies ($f \gg f_0$), the energy becomes

$$E(f) \propto f^{2-2\gamma} f_0^{2\gamma} M_0^2. \tag{5}$$

The seismic moment can be related to the source radius and the dependence of stress drop on source radius. The seismic moment is given by

$$M_0 = \mu A u \propto \mu A \Delta\sigma R \tag{6}$$

Here μ is shear modulus, A is fault area, u is slip, $\Delta\sigma$ is static stress drop, and R is fault radius. The static stress drop is

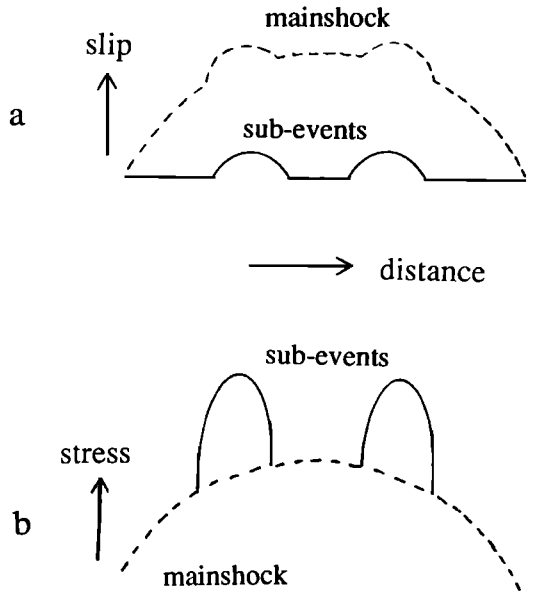

Fig. 3. Schematic plots showing (*a*) slip and (*b*) stress on the fault as a function of distance. (*a*) Dashed line is the slip for main shock that contains two level 1 subevents. Solid line is the slip for the two subevents. The slip shown with the dashed line accumulates over a longer time scale than the slip indicated by the solid line. (*b*) Solid line is initial stress for subevents. Dashed line is long-wavelength component of stress released during the main shock. For the case shown, stress drop is independent of scale length.

proportional to u/R. I let the static stress drop be dependent on source radius such that

$$\Delta\sigma \propto R^{\eta}. \tag{7}$$

I assume that the fault strength is proportional to the stress drop, so that the scaling of stress drop with source radius is identical to the scaling of fault strength with distance on the fault. Substitution into (6) produces

$$M_0 \propto R^{3+\eta}. \tag{8}$$

I assume that the high-frequency energy of the main shock is produced by the subevents. By "high frequency," I am referring to frequencies above the corner frequency of the largest subevent within the main shock. This type of assumption was also made in the works of *Papageorgiou and Aki* [1983], *Joyner and Boore* [1986], and *Boatwright* [1988], all of whom investigated the high-frequency energy of an earthquake composed of multiple subevents of equal radii. In the model presented here, the subevents have a self-similar distribution of sizes. Furthermore, I assume that the high-frequency energy of each subevent is produced by the subevents within it.

The following paragraphs present a qualitative description of how rupture could proceed through a hierarchy of stress/strength variations with different length scales. The results of this paper are not dependent on the sequence or timing of the subevents given here. Figure 3 shows simplified diagrams of how slip and stress could change during the rupture process. Here we consider two different level 1 subevents within a main shock. In this simplified case, I chose two equally-sized subevents. In the general model (Figure 1), there is a distribution of subevent sizes within the subevent. For this example the static stress drop is taken to be the same for the main shock and the subevents. Therefore the maximum slip is proportional to radius. Figure 3 could also represent level $i + 1$ subevents within a level i subevent.

Let rupture nucleate at some point in the main shock rupture zone. The rupture front will expand and encounter the heterogeneous strength along the fault zone. Consider what will happen as rupture propagates into a subevent (Figure 3). Both long wavelength and short wavelength stresses will be relieved as the rupture propagates into the subevent. As it proceeds across the subevent, the rupture front will encounter the small-scale stress variations that will form the subevents and their own subevents. The short-wavelength slip for the subevents is shown in Figure 3*a* as the solid line. As these subevents (and their subevents) are being activated, the longer wavelength slip of the main shock is accumulating (dashed line in Figure 3*a*). The long wavelength slip of the main shock will take longer to build to its final level than the slip of each of the subevents. This time will correspond to the time it takes the rupture front to traverse the rupture zone of the main shock and will be proportional to the rupture dimension of the main shock and inversely proportional to its corner frequency. The total slip for the main shock (dashed curve in Figure 3*a*) will be relatively large at the positions of the subevents. The shorter-wavelength slip for the subevents will be superimposed on the longer-wavelength slip.

When each subevent fails, the stress over its rupture area changes from the solid line in Figure 3*b* to the level of the dashed line. This represents a relatively short wavelength of stress release. Note that Figure 3*b* does not show the zones of small stress increase that would occur at the periphery of the subevent areas after their rupture [see *Andrews*, 1980]. As the mainshock ruptures, the stress drops from the dashed line down to the baseline level, releasing the longer wavelength stress. For this example (Figure 3*b*), the magnitude of the stress change is the same for the subevents and the main shock.

A minimum subevent size is required so that the stress does not become infinite, when the stress drop is independent of scale length. Adding peaks of stress with equal amplitude and smaller and smaller scale lengths (as in Figure 3*b*) would result in an infinite stress if there was no minimum subevent size.

HIGH-FREQUENCY SPECTRAL DECAY AND THE FRACTAL DIMENSION OF SUBEVENTS

I determine the high-frequency falloff of the main shock by evaluating the total high-frequency energy of the level 1 subevents, for frequencies higher than the corner frequency $f_{0\max}$ of the smallest subevent. Here, the term "total energy" refers to the spectral amplitude of the energy at some given frequency for all the level 1 subevents, rather than the energy found from integrating over a range of frequencies. The low-frequency spectral amplitude of the main shock (below the corner frequency) is specified by its seismic moment. The corner frequency of the main shock spectrum is determined by its radius. Given these two constraints, the total high-frequency energy of the subevents for $f > f_{0\max}$ will control the overall falloff of the main shock spectrum for frequencies above the main shock corner frequency.

I assume that the high-frequency energy of the subevents is incoherent, so that their energy is additive [see *Boat-*

wright, 1982]. Therefore the high-frequency energy of the main shock E_{main} can be expressed as the integral of the energy of all of the level 1 subevents, such that

$$E_{main} = \int_{R_{min}}^{R_{max}} E_{sub}\, dN, \tag{9}$$

where E_{sub} is the energy for each level 1 subevent and R_{max} is the radius of the largest subevent. Using (1) and $d(\ln R_{sub}) = R_{sub}^{-1}\, dR_{sub}$, I find

$$dN = pR_{sub}^{-D-1}R_{main}^{D}\, dR_{sub}. \tag{10}$$

Since the concern is with frequencies above the corner frequency of R_{min}, the high-frequency form of the energy spectrum (5) can be used. Substituting (5) and (10) into (9) produces

$$M_{0main}^2 f_{0main}^{2\gamma} f^{2-2\gamma} = p\int_{R_{min}}^{R_{max}} M_{0sub}^2 R_{sub}^{-D-1} R_{main}^{D} f_{0sub}^{2\gamma} f^{2-2\gamma}\, dR_{sub}. \tag{11}$$

Here M_{0main} and M_{0sub} represent the seismic moment of the main shock and subevents, respectively, and f_{0main} and f_{0sub} denote the corner frequencies of the main shock and subevents. Since $f_0 \propto R^{-1}$ and $M_0 \propto R^{3+\eta}$, (11) becomes

$$R_{main}^{6+2\eta-D-2\gamma} = p\int_{R_{min}}^{R_{max}} R_{sub}^{6+2\eta-D-2\gamma-1}\, dR_{sub}. \tag{12}$$

The purpose here is to use (12) to derive an expression for γ, the spectral falloff of the main shock and the subevents. From (12), it is clear that γ is dependent on the constant of proportionality p as well as on D and η. The high-frequency falloff is not uniquely determined by D and η. To specify p, I consider the case where $D = 2$ and the sum of the subevent areas equals the main shock area [also *Boatwright*, 1982]. The total area of the subevents is given by

$$A = \int_{R_{min}}^{R_{max}} \pi R_{sub}^2\, dN. \tag{13}$$

Substitution for dN (10) results in

$$A = pR_{main}^{D}\pi\int_{R_{min}}^{R_{max}} R_{sub}^{-D+1} dR_{sub}. \tag{14}$$

For $D = 2$, I obtain

$$A = p\pi R_{main}^2 (\ln R_{sub})\Big|_{R_{min}}^{R_{max}}. \tag{15}$$

Letting A equal the area of the main shock πR_{main}^2 and rearranging terms yields

$$p = \frac{1}{\ln (R_{max}/R_{min})}. \tag{16}$$

Now substituting this expression for p into (12) results in

$$R_{main}^{6+2\eta-D-2\gamma} = \frac{1}{\ln (R_{max}/R_{min})}\int_{R_{min}}^{R_{max}} R_{sub}^{6+2\eta-D-2\gamma-1}\, dR_{sub}. \tag{17}$$

Equation (17) will be satisfied only if $6 + 2\eta - D - 2\gamma$ equals zero. This can be confirmed by substituting zero for this expression in the exponents on both sides of the equation, producing

$$R_{main}^{0} = \frac{1}{\ln (R_{max}/R_{min})}\int_{R_{min}}^{R_{max}} R_{sub}^{-1}\, dR_{sub}.$$

Both sides of this equation equal one, and the equation is satisfied. Therefore equating the high-frequency energy of the main shock with the integral of the energy of the subevents yields the following expression for the high-frequency falloff:

$$\gamma = 3 + \eta - D/2. \tag{18}$$

Equation (18) indicates that a subevent distribution with $D = 2$ and constant stress drop scaling ($\eta = 0$) will produce a main shock with a falloff of ω^{-2} ($\gamma = 2$) if the subevents fill the main shock rupture area. This is the high-frequency spectral falloff that is typically observed. The analysis above relies on the assumption that the subevents have the same spectral falloff as the main shock. In the next section I show that a $D = 2$ distribution of subevents with falloffs of ω^{-3} results in a main shock with a falloff of about ω^{-2}, for the case of constant stress drop scaling. Again, the subevent areas must fill the area of the main shock. This analysis also applies to producing the high-frequency energy for a level i subevent from the radiation of its constituent level $i + 1$ subevents. R_{max} would then be the largest level $i + 1$ subevent within a particular level i subevent.

COMPOSITE SPECTRUM AT MIDFREQUENCIES

I showed above how the subevent energy sums to the main shock energy for frequencies above the corner frequency of the smallest subevent. The spectral shape of the composite event between the corner frequencies of the largest and smallest subevents was not discussed. For these intermediate frequencies, the radiation of the composite earthquake would be a mix of both coherent and incoherent energy.

As a first approximation, I assume that the subevent energy is incoherent over this frequency range and find the composite spectrum of the level 1 subevents for frequencies above the corner frequency of the largest subevent. Therefore the displacement spectrum of the composite event is proportional to the square root of the integral of the energy of the subevents [*Boatwright*, 1988], so that

$$\Omega_{comp} = \left[\int_{R_{min}}^{R_{max}} \Omega_{sub}^2\, dN\right]^{1/2}, \tag{19}$$

where Ω_{sub} is the displacement spectrum of each level 1 subevent and Ω_{comp} is the displacement spectrum of the composite event. Substituting for Ω_{sub} from (3) and dN from (10) yields

$$\Omega_{comp} = \left[p\int_{R_{min}}^{R_{max}} \frac{M_{0sub}^2 R_{sub}^{-D-1} R_{main}^{D}}{[1 + (f/f_{0sub})^{\gamma}]^2}\, dR_{sub}\right]^{1/2}. \tag{20}$$

The integral in (20) was evaluated numerically at each frequency by summing the integrand over small increments of R_{sub}. Figure 4*a* shows the results for subevents with ω^{-2}, $D = 2$, and $\eta = 0$. Parameter p was given by (16), such that

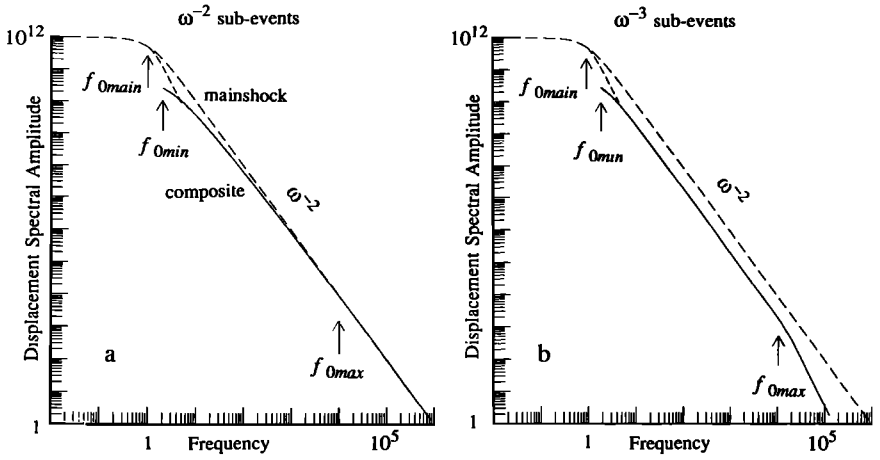

Fig. 4. (a) Solid line is composite displacement spectrum for subevents with $D = 2$, $\eta = 0$, and ω^{-2} obtained from (20). Long-dashed line is the displacement spectrum for the corresponding main shock with the same stress drop as the subevents and a falloff of ω^{-2}. Short-dashed line is the spectrum for the long-wavelength component of slip occurring over the diameter of the main shock rupture (see text). (b) Solid line is composite displacement spectrum for subevents with ω^{-3} ($D = 2$, $\eta = 0$) determined from (20). Dashed lines same as in Figure 4a. For both Figures 4a and 4b, subevents fill main shock rupture zone.

the sum of the subevent areas equals that of the main shock. For both examples depicted in Figure 4, the smallest subevent has a radius 10^{-4} times that of the main shock. The largest subevent has a radius 0.5 times the main shock radius. The f_{0min} is the corner frequency of the largest subevent. Figure 4a also shows the displacement spectrum for the corresponding main shock with the same stress drop as the subevents and an ω^{-2} falloff. This is the spectrum that the composite spectrum of the subevents should approximate.

For frequencies between f_{0min} and f_{0max}, the slope of the composite spectrum is somewhat less than ω^{-2}. At frequencies between f_{0min} and $10f_{0min}$ the falloff is about $\omega^{-1.6}$. The falloff steepens to ω^{-2} as frequency increases. At frequencies above f_{0max}, the high-frequency spectral level of the composite event matches that of the main shock with an ω^{-2} falloff, in accord with the previous section of this paper. If portions of the subevent energy summed coherently, the slope of the composite event would change for frequencies between f_{0min} and f_{0max}. This will tend to steepen the slope of the composite spectrum, since the lower frequency energy will tend to sum coherently, producing larger spectral amplitudes at lower frequencies. A more accurate method for determining the composite spectrum between f_{0min} and f_{0max} is to sum the subevent radiation in the time domain using time delays determined by a stochastic rupture simulation [e.g., *Boatwright*, 1988]. Such a simulation is beyond the scope of this paper.

The spectrum of the composite event must also include the contribution from slip with a half-wavelength corresponding to the diameter of the main shock rupture zone (dashed line in Figure 3a). This long-wavelength slip accounts for most of the moment of the main shock. In Figure 4, I represent this component by a spectrum with the low-frequency level and corner frequency of the main shock (short-dashed line in Figure 4a). For illustrative purposes, I choose a spectral falloff of ω^{-3} for this long-wavelength component of slip, consistent with rupture nucleation and smooth propagation. For this falloff the spectral amplitude produced by the long-wavelength component of slip intersects the composite spectrum of the subevents at a frequency just above the f_{0min} (Figure 4).

Thus the composite event would have a falloff of about ω^{-3} for frequencies between the corner frequencies of the main shock and the largest subevent and falloffs less steep than ω^{-2} for frequencies between f_{0min} and f_{0max}, for this summation procedure. The overall falloff of the composite spectrum is ω^{-2}, for frequencies above the corner frequency of the main shock.

Figure 4b contains the composite displacement spectrum for subevents with ω^{-3} falloffs. Again $D = 2$, $\eta = 0$ and the subevents fill the main shock area. The falloff of the composite spectrum equals ω^{-2} for frequencies between the corner frequencies of the largest and smallest subevents. Above the corner frequency of the smallest subevent, the composite spectrum falls off as ω^{-3}. As in the previous example, I include the spectrum for the long-wavelength component of slip corresponding to the main shock rupture diameter as the short-dashed line in Figure 4b. If one determines a spectral falloff for the composite event using the spectral amplitude of the composite event at f_{0max} and the spectral amplitude of the main shock at f_{0main}, the overall falloff of the composite spectrum approaches ω^{-2}.

The composite spectra demonstrate that subevents with falloffs of ω^{-2} or ω^{-3} will produce a composite event with an high-frequency falloff of approximately ω^{-2}, if $D = 2$, $\eta = 0$, and the subevents fill the main shock rupture zone.

Fractal Dimension of Subevents and the Scaling of Fault Strength With Distance

In this section, I show how the fractal dimension of the subevents is a consequence of the scaling of fault strength with distance on the fault, so that D and η are related. Following *Hanks* [1979] and *Andrews* [1980], I consider stress to be a self-similar random function of position on the fault. Figure 5 shows a perspective plot of a realization of stress that varies in a self-similar, random manner on a fault plane. The height of the topography is proportional to the stress above some average value. The "water level" repre-

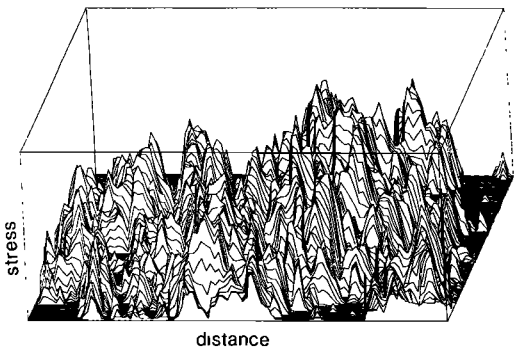

Fig. 5. Perspective plot of a realization of random, self-similar stress along a fault plane. The height of the topography is proportional to the stress at that position on the fault plane. The zero level corresponds to the average stress. Areas with below-average stress are zeroed. When sampled along a line, the example shown here produces self-similar random traces with $H = \eta = 0.5$.

sents the average stress. For this plot, I have zeroed values of stress less than the average. The construction of this self-similar model is described below.

If one samples the stress along any particular line in the fault plane, the resulting function is self-similar. The traces in Figure 6 are two examples of self-similar random functions that could represent stress along a line within a fault plane. These random functions have a Gaussian distribution of stress about some average value. Their construction is detailed later in this section. Self-similarity means that if one took a small segment of the trace with Δx and expanded it along the x axis to equal the horizontal extent x of the original trace, it would be statistically identical to the original trace, scaled in amplitude by the factor $(\Delta x/x)^H$ [*Mandelbrot*, 1977]. H is called the Hurst exponent and has values between zero and one. Traces with smaller values of H have

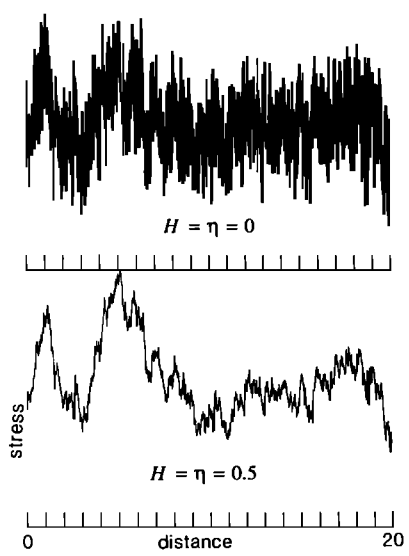

Fig. 6. Two examples of self-similar, random functions representing stress sampled along a line in a fault plane. The top trace has $H = \eta = 0$, a power spectrum proportional to $1/k$ ($D = 2$), and a stress drop independent of scale length. The bottom trace has $H = \eta = 0.5$, a power spectrum proportional to k^{-2}, and a stress drop that decreases with smaller length scales. Distance is given in arbitrary units.

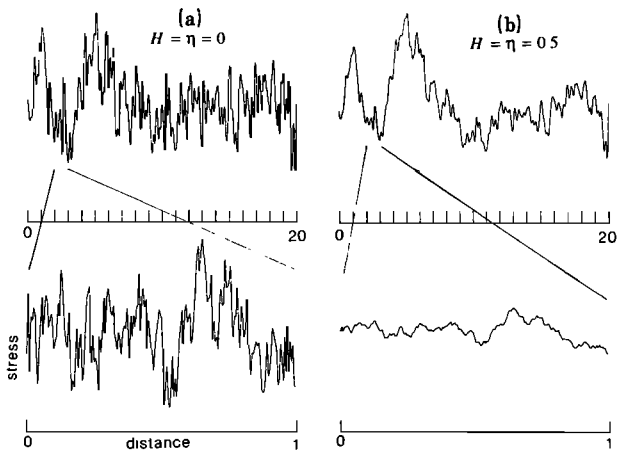

Fig. 7. Plots of self-similar random functions at two different length scales. The traces are plotted such that there is equal resolution for each length scale, relative to the total length of each plot (see text). The traces on each side of the figure are plotted on the same vertical scale. The original traces are shown in Figure 6. (*a*) Traces for $H = \eta = 0$, and the standard deviation is independent of scale length as shown by the equal amplitudes of the top and bottom traces. (*b*) Traces for $H = \eta = 0.5$, and the standard deviation decreases as the scale length decreases.

rougher character. The traces in Figure 6 have H values of 0 and 0.5.

Following *Andrews* [1980], I assume that the average stress drop over an area on the fault is proportional to the standard deviation of the spatial variations in stress over that area. The standard deviation of stress describes the average amplitude of the stress variations. Rupture of a main shock or subevent removes the spatial fluctuation in stress over the dimension of the main shock or subevent rupture zone (see also Figure 3*b*). Thus the stress drop will be about equal to the amplitude of the stress variation and proportional to the standard deviation of the stress variations.

Since the standard deviation scales with the amplitude of a trace, the standard deviation of a self-similar trace will be proportional to R^H, where R is the distance sampled. The stress drop averaged over some rupture zone with radius R will be

$$\Delta\sigma \propto R^H. \tag{21}$$

Thus H describes the scaling of stress drop with source radius and is equal to η (see (7)).

Figure 7 illustrates how the standard deviations of self-similar functions scale with distance sampled. Here I show two self-similar functions viewed at two different length scales that vary by a factor of 20. The traces in this figure were derived from the functions in Figure 6. In Figure 7, each function is displayed at two different length scales such that the resolution in each plot is equal, relative to the total length of that plot. For each of the top traces, this was accomplished by low-pass filtering the corresponding function in Figure 6. Each bottom trace is a short sample of the corresponding function in Figure 6.

For the case with $H = 0$ (Figure 7*a*) we see that the standard deviation of stress does not change significantly with length scale. The bottom trace in Figure 7*a* has about the same standard deviation as the top trace. For this case, the stress drop or strength is independent of scale length and

η equals 0. In Figure 7b, H equals 0.5, and the standard deviation of stress decreases as the scale length is decreased. Now the stress drop will decrease as smaller portions of the fault are considered. For this case, the stress drop will be proportional to $R^{0.5}$.

Let the top trace in Figure 8 represent stress sampled along a line in a fault plane. The trace shown has $H = \eta = 0.5$. I define the rupture zones of the main shocks on the fault as areas where the stress on the fault plane is above average (the zero level of the plot). Thus the rupture zone lengths are delimited by the zero crossings. I chose this definition of rupture length because the distance between zero crossings of a self-similar function defines a fractal set [*Mandelbrot*, 1977]. If we view the stress as a topographic surface whose height varies in a self-similar manner as a function of position on the fault plane (Figure 5), the rupture zone areas would correspond to islands whose rupture zone perimeters are their coastlines. *Mandelbrot* [1977, p. 231] states that the number of islands with areas greater than A is

$$N(A) \propto A^{-(2-H)/2}. \tag{22}$$

Here H is the Hurst exponent of any trace found from taking a section of the topographic surface. The choice of water level is arbitrary and does not affect this relation. Since area is proportional to R^2, this equation becomes

$$N(R) \propto R^{-(2-H)}. \tag{23}$$

Thus the size distribution of rupture zones on the fault plane is controlled by the value of H for the self-similar traces that describe the stress variations on the fault plane. Comparing the forms of (2) and (23), we find that

$$D = 2 - H = 2 - \eta. \tag{24}$$

Here D describes the size distribution of rupture zones on a fault. I will show below that (24) is also valid for characterizing the size distribution of subevents within the main shock and within other subevents.

Equation (24) states that the size distribution of rupture zones on a fault (defined by zero crossings) is controlled by the scaling of strength on the fault. This point will be utilized in the section on b value.

I assume that the subevent areas correspond to small-scale perturbations of stress on the fault plane. Figure 8 illustrates how subevents at various levels can be identified in a self-similar random function of stress. Consider one of the main shock rupture zones defined by two of the zero crossings in the top trace of Figure 8. The level 1 subevents for this main shock are shown in the middle trace of Figure 8. This trace was obtained by high-pass filtering the stress function of the top trace with a corner wavelength equal to about twice the rupture diameter of the main shock. This filtering removes the long-wavelength "hill" of stress that represents this particular main shock rupture area in the top trace. I define the level 1 subevents as the portions of the middle trace of Figure 8 that are above the zero level. A similar procedure can be used to isolate the level 2 subevents in one of these level 1 subevents. The bottom trace in Figure 8 is a portion of the middle trace that was high-pass filtered with a corner wavelength that is about twice the diameter of the level 1 subevent selected. The level 2 subevents are the areas above the zero level in the bottom trace.

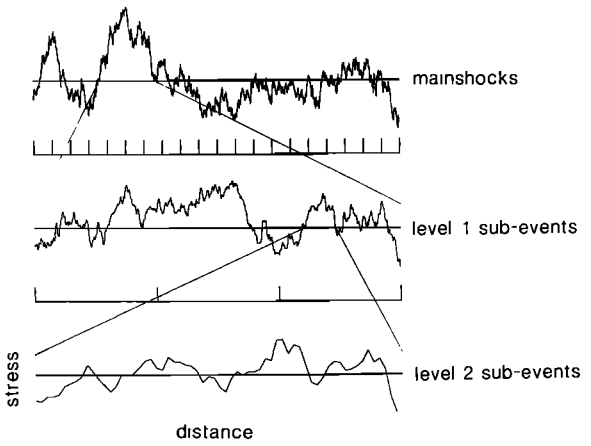

Fig. 8. Plots of different portions of a self-similar function illustrating main shock rupture areas and subevents on level 1 and 2 (see Figure 1). The function represents the random component of stress along a fault. The zero level (horizontal line on each plot) is the average stress. The plots are normalized to the peak amplitude of the trace in each plot. In the top trace, main shock rupture zones are taken to be areas above the zero level. The middle and lower traces are successive blow-ups of portions of the upper trace, after high-pass filtering to remove the long-period component of stress (see text). The middle trace shows the level 1 subevents (areas above horizontal line) within one of the main shock rupture areas. The bottom trace depicts level 2 subevents within one of the level 1 subevents. This particular example has $H = \eta = 0.5$.

The size distribution of the subevents at any level of rupture obeys the relationship in (23). If we take a small portion of a self-similar trace and expand it horizontally, the slope of the original long-period trend can be reduced until it is essentially horizontal. The subevents riding on the long-period trend will now be the areas on the trace above this horizontal line. Because of self-similarity, the size distribution of the subevents, as defined by the crossings of this horizontal line, will be identical to the size distribution of the zero crossings of the original trace. The size distribution for the subevents must be identical to the size distribution describing the zero crossings, that is, (23).

Thus the size distribution of subevents within the main shock or subevents within other subevents is controlled by the scaling of strength (stress drop) on the fault, when the subevents are defined in the manner described above. Equation (24) relates the fractal dimension D of the subevent distribution to the scaling of strength on the fault. When the fault strength is scale invariant ($H = \eta = 0$), D is equal to 2 and the number of subevents is inversely proportional to their area.

Figure 9 shows map views of two realizations of subevents on a main shock rupture zone. This figure illustrates how the size distribution of subevents is related to the scaling of strength (η) on the fault plane. These realizations were derived from two-dimensional self-similar functions that were high-pass filtered to remove the long-wavelength components with wavelengths comparable to the length of the main shock rupture zone (i.e., the length of one of the sides in Figure 9). Darkened areas in Figure 9 are portions of the fault plane with higher than average stress, and the white areas represent lower than average stress. Therefore the level 1 subevent rupture areas appear as black islands with various sizes and geometries along the fault plane. The two

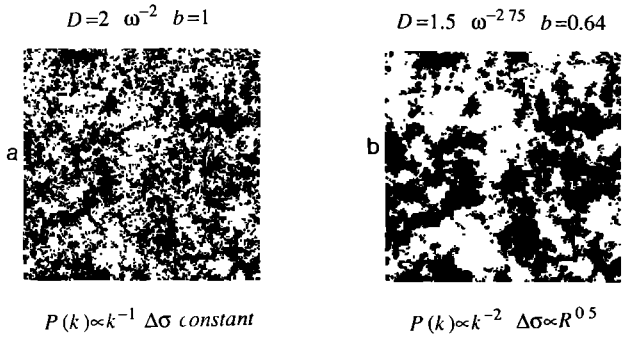

Fig. 9. Shaded map views of two examples of self-similar random stress along a fault plane. Darkened areas have higher than average stress and are taken to be the rupture areas of subevents. White areas have lower than average stress. These pictures of subevent areas can be compared to the more schematic model of subevents shown in Figure 1. Shown with each example are the one-dimensional power spectrum $P(k)$, the fractal dimension D, and the high-frequency spectral falloff $\omega^{-\gamma}$ for that example, for $p = [\ln (R_{max}/R_{min})]^{-1}$. Also written by each panel are the b values found if the shaded areas are interpreted as rupture zones of aftershocks.

examples shown in Figure 9 differ in their size distribution of subevents, with Figure 9b ($\eta = 0.5$) having fewer subevents with smaller areas than Figure 9a ($\eta = 0$).

For the case when the subevents fill the main shock rupture area, the rupture area of each subevent must be larger than the area of the corresponding island of high stress. The analysis above only requires the subevent rupture area to be proportional to the area of the island of high stress. It is reasonable to expect the final rupture size of each subevent (R_{sub}) to exceed the area of the island.

D, η, and H are related to the high-wave number falloff of the power spectrum of the self-similar trace. This was demonstrated by *Andrews* [1980], and the procedure in the next paragraphs follows his work. For a self-similar random function, the one-dimensional power spectrum $P(k)$ must be a power function of the wave number k, where $k = 2\pi/\lambda$ and λ is the wavelength, such that

$$P(k) \propto k^{-n}. \tag{25}$$

The relationship between n and H can be found from calculating the standard deviation of the random stress function after it has been band-pass filtered between certain wavelengths. By band-pass filtering the random trace, we can look at the variation of stress over different length scales. Since the standard deviation of the band-pass-filtered function increases with the bandwidth of the filter, it is necessary to band-pass filter over equal logarithmic intervals (e.g., octaves) of wavelength when comparing the standard deviation at different length scales. This is a consequence of the definition of self-similarity. A self-similar function has the same statistics after logarithmic changes in scale length. Only by using equal logarithmic intervals between the lower and upper limits of each band-pass filter will the upper limits of different filters scale by the same factor as the lower limits and the center wavelengths.

To estimate the standard deviation of a band-pass-filtered trace, I calculate the standard deviation s of stress over an octave interval of wavelength along the fault. The variance s^2 of a function after it has been band-pass filtered between an octave interval of wavelength can be found from

$$s^2 \propto \int_{k_0}^{2k_0} P(k)\, dk \tag{26}$$

Here k_0 is inversely proportional to some wavelength (λ) or scale length on the fault. The limits of integration k_0 and $2k_0$ correspond to an octave interval of the wavelength on the fault.

By integrating (26), we can find the scaling of the stress drop (or strength) with distance as a function of the exponent n of the power spectrum of the stress drop trace. As described above, we equate the dependence of the standard deviation of the stress on scale length λ to the dependence of stress drop on source radius R. Thus k_0 will be inversely proportional to R. Substitution from (25) and integration produces

$$\begin{aligned} s^2 &\propto k_0^{-n+1} \propto R^{n-1} \qquad n \neq 1 \\ s^2 &\propto \ln (2k_0/k_0) = \ln 2 \qquad n = 1. \end{aligned} \tag{27}$$

Therefore the standard deviation of stress s over a distance R is proportional to $R^{(n-1)/2}$. Letting the stress drop be proportional to the standard deviation of stress, we have

$$\Delta\sigma \propto R^{(n-1)/2}. \tag{28}$$

Comparing this expression with the right side of (7), we see that

$$H = \eta = (n - 1)/2. \tag{29}$$

Thus the scaling of stress drop with source size is related to the exponent of the power spectrum of the stress drop. Note that for $P(k) = k^{-1}$ ($n = 1$), the average stress drop is independent of source size and the average fault strength is independent of scale length ($H = \eta = 0$; see also *Andrews* [1980]).

The two-dimensional self-similar models in Figures 5 and 9 and the self-similar traces in Figures 6–8 were constructed by specifying their power spectra in the wave number domain. Each self-similar trace was made by filtering a sequence of Gaussian random numbers in the wave number domain so that its power spectrum corresponded to (25). The values of n were derived from (29). The original random number sequence had a white spectrum. Both the original and filtered sequences have a Gaussian distribution about the mean.

For the two-dimensional models, a Gaussian random number generator was used to assign a value for each point in a two-dimensional grid. This grid was transformed to the wave number domain (k_x, k_y) with a two-dimensional Fourier transform. In the wave number domain, the spectra were filtered so that their two-dimensional power spectra were of the form

$$P_{2D}(k_r) \propto k_r^{-n-1}. \tag{30}$$

Here k_r is the radial wave number. The filtered spectra were then transformed back into the spatial domain. Note that when a two-dimensional function with a power spectrum given by (30) is sampled along a line, the one-dimensional power spectrum of the resulting trace will be given by (25). Further details on the construction of two-dimensional, random functions are given by *Frankel and Clayton* [1986].

HIGH-FREQUENCY SPECTRAL FALLOFF AND THE SCALING OF FAULT STRENGTH

We can use (24) to replace D in (18) and find γ as a function only of η, the dependence of stress drop on radius. The result is

$$\gamma = 2 + 1.5\eta. \tag{31}$$

In terms of fractal dimension, we find

$$\gamma = 5 - 1.5D. \tag{32}$$

These expressions define the falloff for a particular scaling of strength along the fault. These formulas presuppose that $p = [\ln (R_{max}/R_{min})]^{-1}$.

When the stress drop is independent of source radius (and seismic moment), $\eta = 0$, D is 2, and the spectral falloff is ω^{-2}. The last result was also found by *Hanks* [1979] and *Andrews* [1981]. This corresponds to a faulting model where the number of subevents is proportional to the ratio between the areas of the main shock and a subevent (equation (1) with $D = 2$). *Boatwright* [1982, 1988] and *Joyner and Boore* [1986] have previously reported that such a summation process produces an ω^{-2} falloff. The work presented here indicates that the ω^{-2} falloff that is typically observed for earthquake displacement spectra can be a direct result of the scale invariance of strength along fault zones.

This model of complex rupture predicts that spectral falloffs steeper than ω^{-2} can be produced in two ways. First, if $D = 2$ and the subevents do not fill up the area of the main shock, then p is less than $[\ln (R_{max}/R_{min})]^{-1}$. This would lower the absolute amplitude of the composite spectrum in Figure 4*a*, producing less high-frequency energy. A main shock with an overall falloff steeper than ω^{-2} for frequencies between f_{0main} and f_{0max} will result.

When the stress drop increases with moment ($\eta > 0$), the spectral falloff can also be steeper than ω^{-2}. In this case, D is less than 2 and there will be fewer small subevents relative to large subevents (see Figure 9). This will produce less high-frequency energy compared to $D = 2$, for the same value of p. Given the same p value, distributions with $D < 2$ ($\eta > 0$) will produce main shocks and subevents with steeper high-frequency falloffs than the case with scale-invariant strength. For the stress field shown in Figure 9*b* with $\eta = 0.5$ and $D = 1.5$, the high-frequency falloff is $\omega^{-2.75}$ for $p = [\ln (R_{max}/R_{min})]^{-1}$ (see equation (31)).

THE b VALUES OF AFTERSHOCK SEQUENCES AND THE SCALING OF STRENGTH ON FAULTS

The self-similar model for subevents shown in Figure 1*a* can also be applied to the rupture zones of individual earthquakes on a fault, to arrive at an expression between the b value and the scaling of stress on the fault. The frequency-magnitude relation can be expressed as

$$\log N = a - bM. \tag{33}$$

Here N is the number of events occurring over some period of time with magnitudes greater than M, and a is a constant.

Determining the b value from the size distribution of rupture zones requires an assumption about how often individual rupture areas produce earthquakes during a given time period. If each rupture zone had the same repeat time regardless of its area, the b value for a fault would simply reflect the number versus size characteristics of the rupture areas. The validity of this assumption is not obvious. Some model for the loading of faults or fault segments would be needed to establish the recurrence intervals for faults or fault segments of different sizes.

For an aftershock sequence occurring on a fault, however, it is reasonable to postulate that the size distribution of aftershock rupture zones directly controls the b value. Such aftershocks are thought to occur on patches of high stress that are loaded by the failure of the main shock. Once one particular aftershock fails, it seems unlikely that it will fail again in that aftershock sequence. It will no longer be loaded. This is similar to what would occur for subevents within an earthquake. Once a particular subevent fails, it will probably not rupture again during that earthquake. If each aftershock rupture zone fails only once in a given sequence, then the size distribution of rupture zones corresponds to the number of aftershocks observed over a period of time as a function of rupture area or magnitude.

In this section, I show that the b value of aftershock sequences is controlled by the scaling of strength on a fault. I use a model with a self-similar distribution of aftershock rupture zones on a fault, as in Figure 1*a*. Again the strength of the fault is assumed to be described by a random self-similar function such as those in Figure 8. I assume that aftershocks occur in areas where the strength along the fault zone exceeds some threshold value. Aftershocks within the rupture zone of the main shock could be interpreted as subevents that do not rupture during the main shock, but fail in a time-dependent manner afterward. Thus the above analysis relating the scaling of fault strength to the size distribution of subevent rupture areas is also applicable to the size distribution of aftershock rupture areas. Let the number of aftershocks with radii greater than R be proportional to R^{-D}. The fractal dimension D describing the size distribution of the aftershock rupture areas will equal $2 - \eta$.

Now I derive the relation between b value and the fractal dimension D. It is typically observed [e.g., *Thatcher and Hanks*, 1973; *Kanamori and Anderson*, 1975] that $\log M_0 = 1.5M + C$, where M is either the local magnitude or surface wave magnitude and C is a constant. Using other magnitude-moment relations would alter the following equations. After substitution for M, (33) becomes

$$\log N = c - \frac{b}{1.5} \log M_0 \tag{34}$$

Since M_0 is proportional to $R^{3+\eta}$ (equation (7)), (34) yields

$$\log N = d - \frac{(3 + \eta)b}{1.5} \log R. \tag{35}$$

Comparing this equation with (2), we see that

$$D = (3 + \eta)b/1.5 \tag{36}$$

or

$$b = 1.5D/(3 + \eta). \tag{37}$$

Using the relation between D and η (equation (24)), produces

$$b = \frac{3 - 1.5\eta}{3 + \eta} . \quad (38)$$

Hanks [1979] previously suggested that stress drop scaling with moment and b value should be related. Here I have quantified the relation.

Thus when stress drop is independent of source size ($\eta = 0$), the b value is equal to 1 (equation (38)). This value is similar to the average b value reported for various aftershock sequences [e.g., *Utsu*, 1971]. The b value of 1 is simply a reflection of stress drop or crustal strength being independent of length scale. We have demonstrated above that a scale-invariant fault strength creates a distribution of rupture sizes where the number of earthquakes with any given rupture area is inversely proportional to that area (see also Figure 9*a*).

Many other studies have shown that if the number of rupture areas is inversely proportional to their area, the b value is 1 [*Kanamori and Anderson*, 1975; *Hanks*, 1977; *Andrews*, 1980; *Aki*, 1981; *Turcotte*, 1989; *Rundle*, 1989]. However, these studies implicitly assumed that the repeat time of any given fault or fault segment is independent of its size. I only consider the b value of aftershock sequences to obviate this problem. It is intriguing, though, that b values taken over a large region generally are about 1. This may imply that the recurrence interval is, on average, independent of the rupture size when earthquakes occurring in a large region are considered.

When the strength or stress drop increases with distance ($\eta > 0$), (38) predicts that the b value will be less than 1. In this instance, there will be relatively fewer small rupture zones compared to large ones, than for the case with scale-invariant stress. Note the b values shown in Figures 9*a* and 9*b*. The aftershock subevent distribution in Figure 9*b* corresponds to a b value of 0.64. When the stress drop decreases with increasing length ($\eta < 0$), the b value will be greater than 1.

DISCUSSION

This paper demonstrates how a spectral falloff of ω^{-2} and a b value of 1 for aftershock sequences can be a consequence of strength that is scale-invariant along a fault plane. The question remains as to whether scale invariance of strength is valid for all faults and all length scales. Perhaps the strongest evidence for scale-invariant strength on faults is from the scaling of earthquake stress drops with rupture dimension. There are many studies which have shown that earthquake stress drops are generally independent of source dimension and seismic moment for earthquakes above magnitude 3 [*Aki*, 1967; *Kanamori and Anderson*, 1975; *Hanks*, 1977]. For smaller events, it is crucial that proper corrections for path effects (e.g., the site response) be applied before determining the source radius and stress drop from the pulse widths or corner frequencies. *Frankel and Wennerberg* [1989] found that stress drop remained constant with moment for two events at Anza, California, with magnitudes of 1.4 and 3.1. Many more studies of stress drop scaling of small earthquakes must be done using empirical path corrections to remove the effects of site response.

The results of this paper indicate that the overall high-frequency falloff of a main shock composed of subevents may not be directly related to the physics of dynamic rupture. The model presented here implies that the falloff is essentially determined by the size distribution and stress drop scaling of the subevents. An ω^{-2} falloff will result for $D = 2$ and $\eta = 0$ regardless of whether the falloff of the constituent subevents is ω^{-2} or ω^{-3}, if the subevents fill the area of the main shock (Figure 4). Of course, the physics of dynamic rupture ultimately controls whether the subevents will fill the area of the main shock. Furthermore, the summation of the subevent spectra for frequencies between $f_{0\min}$ and $f_{0\max}$ is a consequence of the timing of the subevents and hence of the rupture dynamics.

This self-similar model of earthquake rupture has implications to how the radiation from large earthquakes can be simulated by summing the waveforms of smaller earthquakes. One problem with these simulations has been the difficulty of matching both the high-frequency and low-frequency spectral amplitudes of the larger event by simply summing up the waveforms of a smaller event [see *Boatwright*, 1988]. Figure 3*a* illustrates one way of viewing the problem. The slip of the subevents by themselves cannot account for the total slip of the main shock. However, I postulated that the total high-frequency radiation from these subevents accounts for the high-frequency energy of the main shock. When summing up the radiation from small events to make that of a larger event, it is necessary to add low-frequency energy so that the slip of the larger event is duplicated. In Figure 4 this was accomplished by adding a long-wavelength component of slip with a spectrum indicated by the short-dashed lines. *Boatwright* [1988] addresses this problem by low-pass filtering the waveforms of the small events before they are summed to simulate a larger event. This filtering essentially boosts the low-frequency energy of the small events relative to their high-frequency energy.

It has been reported that aftershocks of large earthquakes generally do not occur in portions of the fault where most of the slip was released during the main shock [e.g., *Doser and Kanamori*, 1986; *Mendoza and Hartzell*, 1988]. Such behavior is consistent with the self-similar model of subevents shown in Figure 1*a*. If stress drop is constant or increases with source radius, areas of the fault plane with the largest subevents will have the largest slip (see Figure 3*a*). These largest subevents would correspond to the "asperities" often found in the analysis of teleseismic and local records for large earthquakes. Aftershocks may be located on high-strength patches on the fault that did not rupture during the main shock. If this is the case, the aftershock rupture areas should not be located in the subevent areas of the main shock, including the largest subevents which produced most of the slip.

The predictions and validity of the self-similar model of rupture presented in this paper should be evaluated with numerical simulations of dynamic rupture propagation using realistic relations for fault friction [e.g., *Okubo*, 1989]. Such simulations should consider rupture growth and stopping behavior when the fault strength and stress are self-similar random functions, incorporating variations on a variety of length scales.

Acknowledgments. I am grateful to D. J. Andrews for comments on an early version of the paper which led me to substantially revise it. He noted the proper form for the distribution function and the importance of the Hurst exponent in describing self-similar functions. Tom Hanks provided many useful comments on the original

manuscript, prompting me to significantly expand its scope and include the section on b values. Suggestions by Kojiro Irikura and John Anderson led to substantial improvement of the paper. I thank Tom Heaton, Paul Richards, and Keiiti Aki for helpful comments. I have benefited from discussions about earthquake source processes with Jack Boatwright, David Boore, Jim Mori, Paul Okubo, Art McGarr, John Unger, and Edward Cranswick.

REFERENCES

Aki, K., Scaling law of seismic spectrum, *J. Geophys. Res.*, *72*, 1217–1231, 1967.

Aki, K., A probabilistic synthesis of precursory phenomena, in *Earthquake Prediction: An International Review*, *Geophys. Monogr. Ser.*, vol. 4, edited by D. W. Simpson and P. G. Richards, pp. 566–574, AGU, Washington, D. C., 1981.

Andrews, D. J., A stochastic fault model, 1, Static case, *J. Geophys. Res.*, *85*, 3867–3877, 1980.

Andrews, D. J., A stochastic fault model, 2, Time-dependent case, *J. Geophys. Res.*, *86*, 10,821–10,834, 1981.

Aviles, C. A., C. H. Scholz, and J. Boatwright, Fractal analysis applied to characteristic segments of the San Andreas Fault, *J. Geophys. Res.*, *92*, 331–344, 1987.

Blandford, R. R., A source theory for complex earthquakes, *Bull. Seismol. Soc. Am.*, *65*, 1385–1405, 1975.

Boatwright, J., A dynamic model for far-field accelerations, *Bull. Seismol. Soc. Am.*, *72*, 1049–1068, 1982.

Boatwright, J., The seismic radiation from composite models of faulting, *Bull. Seismol. Soc. Am.*, *78*, 489–508, 1988.

Boatwright, J., and H. Quin, The seismic radiation from a three-dimensional dynamic model of a complex rupture process, I, Confined ruptures, in *Earthquake Source Mechanics*, *Geophys. Monogr. Ser.*, vol. 6, edited by S. Das et al., pp. 97–110, AGU, Washington, D. C., 1986.

Brown, S. R., and C. H. Scholz, Broad bandwidth study of the topography of natural rock surfaces, *J. Geophys. Res.*, *90*, 12,575–12,582, 1985.

Brune, J. N., Tectonic stress and the spectra of seismic shear waves, *J. Geophys. Res.*, *75*, 4997–5009, 1970.

Chael, E. P., Spectral scaling of earthquakes in the Miramichi region of New Brunswick, *Bull. Seismol. Soc. Am.*, *77*, 347–365, 1987.

Dieterich, J. H., A model for nucleation of earthquake slip, in *Earthquake Source Mechanics*, *Geophys. Monogr. Ser.*, vol. 6, edited by S. Das et al., pp. 37–48, AGU, Washington, D. C., 1986.

Doser, D. I., and H. Kanamori, Depth of seismicity in the Imperial Valley region (1977–1983) and its relationship to heat flow, crustal structure, and the October 15, 1979, earthquake, *J. Geophys. Res.*, *91*, 675–688, 1986.

Frankel, A., and R. W. Clayton, Finite difference simulations of seismic scattering: Implications for the propagation of short-period seismic waves in the crust and models of crustal heterogeneity, *J. Geophys. Res.*, *91*, 6465–6489, 1986.

Frankel, A., and L. Wennerberg, Microearthquake spectra from the Anza, California, seismic network: Site response and source scaling, *Bull. Seismol. Soc. Am.*, *79*, 581–609, 1989.

Hanks, T. C., Earthquake stress drops, ambient tectonic stresses, and stresses that drive plate motions, *Pure Appl. Geophys.*, *115*, 441–458, 1977.

Hanks, T. C., *b* values and $\omega^{-\gamma}$ seismic source models: Implications for tectonic stress variations along active crustal fault zones and the estimation of high-frequency strong ground motion, *J. Geophys. Res.*, *84*, 2235–2242, 1979.

Hanks, T. C., The corner frequency shift, earthquake source models, and *Q*, *Bull. Seismol. Soc. Am.*, *71*, 597–612, 1981.

Haskell, N. A., Total energy and energy spectral density of elastic wave radiation from propagating faults, *Bull. Seismol. Soc. Am.*, *54*, 1811–1841, 1964.

Housner, G. W., Characteristics of strong-motion earthquakes, *Bull. Seismol. Soc. Am.*, *37*, 19–31, 1947.

Housner, G. W., Properties of strong ground motion earthquakes, *Bull. Seismol. Soc. Am.*, *45*, 197–218, 1955.

Joyner, W. B., and D. M. Boore, On simulating large earthquakes by Green's-function addition of smaller earthquakes, in *Earthquake Source Mechanics*, *Geophys. Monogr. Ser.*, vol. 6, edited by S. Das et al., pp. 269–274, AGU, Washington, D. C., 1986.

Kanamori, H., and D. L. Anderson, Theoretical basis of some empirical relations in seismology, *Bull. Seismol. Soc. Am.*, *65*, 1073–1096, 1975.

Madariaga, R., Dynamics of expanding circular faults, *Bull. Seismol. Soc. Am.*, *66*, 639–667, 1976.

Madariaga, R., High-frequency radiation from crack (stress drop) methods of earthquake faulting, *Geophys. J. R. Astron. Soc.*, *51*, 625–651, 1977.

Mandelbrot, B. B., *Fractals*, 365 pp., W. H. Freeman, New York, 1977.

Mendoza, C., and S. H. Hartzell, Aftershock patterns and main shock faulting, *Bull. Seismol. Soc. Am.*, *78*, 1438–1449, 1988.

Okubo, P. G., Dynamic rupture modeling with laboratory-derived constitutive relations, *J. Geophys. Res.*, *94*, 12,321–12,335, 1989.

Okubo, P. G., and K. Aki, Fractal geometry in the San Andreas Fault system, *J. Geophys. Res.*, *92*, 345–356, 1987.

Papageorgiou, A. S., and K. Aki, A specific barrier model for the quantitative description of inhomogeneous faulting and the prediction of strong ground motion, *Bull. Seismol. Soc. Am.*, *73*, 693–720, 1983.

Richter, C. F., *Elementary Seismology*, W. H. Freeman, New York, 1958.

Rundle, J. B., Derivation of the complete Gutenberg-Richter magnitude-frequency relations using the principle of scale-invariance, *J. Geophys. Res.*, *94*, 12,337–12,342, 1989.

Scholz, C. H., and C. A. Aviles, The fractal geometry of faults and faulting, in *Earthquake Source Mechanics*, *Geophys. Monogr. Ser.*, vol. 6, edited by S. Das et al., pp. 147–155, AGU, Washington, D. C., 1986.

Smalley, R., D. Turcotte, and S. Solla, A renormalization group approach to the stick-slip behavior of faults, *J. Geophys. Res.*, *90*, 1894–1900, 1985.

Tchalenko, J. S., and N. N. Ambraseys, Structural analysis of the Dasht-e-Bayaz (Iran) earthquake fractures, *Geol. Soc. Am. Bull.*, *81*, 41–60, 1970.

Thatcher, W., and T. C. Hanks, Source parameters of southern California earthquakes, *J. Geophys. Res.*, *78*, 8547–8576, 1973.

Turcotte, D. L., Fractals in geology and geophysics, *Pure. Appl. Geophys.*, *131*, 171–196, 1989.

Utsu, T., Aftershocks and earthquake statistics, III, *J. Fac. Sci. Hokkaido Univ., Ser. VII*, *3*, 379–441, 1971.

A. Frankel, U.S. Geological Survey, 922 National Center, Reston, VA 22092.

(Received May 25, 1990;
revised January 7, 1991;
accepted January 7, 1991.)